Electronic structure and site occupancy of lanthanide-doped (Sr, ca)$_3$(Y, lu)$_2$Ge$_3$O$_{12}$ garnets

A spectroscopic and first-principles study

Luo, Hongde; Ning, Lixin; Dong, Yuanyuan; Bos, Adrie J.J.; Dorenbos, Pieter

DOI
10.1021/acs.jpcc.6b09077

Publication date
2016

Document Version
Accepted author manuscript

Published in
Journal of Physical Chemistry C

Electronic Structure and Site Occupancy of Lanthanides Doped (Sr, Ca)$_3$(Y, Lu)$_2$Ge$_3$O$_{12}$ Garnets: A Spectroscopic and First-Principles Study

Hongde Luo[a*], Lixin Ning[b], Yuanyuan Dong[b], Adrie J.J Bos[a], Pieter Dorenbos[a]

[a] Delft University of Technology, Faculty of Applied Sciences, Department of Radiation Science and Technology (FAME-RST), Mekelweg 15, 2629JB Delft, The Netherlands

E-mail: h.luo@tudelft.nl

[b] Department of Physics, Anhui Normal University, Wuhu, Anhui 241000, China

Abstract:

Photoluminescence excitation (PLE) and emission spectra (PL) of undoped (Sr, Ca)$_3$(Y, Lu)$_2$Ge$_3$O$_{12}$ as well as Eu^{3+} and Ce^{3+} doped samples have been investigated. The PL spectra show that Eu^{3+} enters into both dodecahedral (Ca, Sr) and octahedral (Y, Lu) sites. Ce^{3+} gives two broad excitation bands in the range of 200 to 450 nm. First principle calculations for Ce^{3+} on both dodecahedral and octahedral sites provide sets of 5d excited level energies that are consistent with the experimental results. Then the vacuum referred binding energy diagrams for (Sr, Ca)$_3$(Y, Lu)$_2$Ge$_3$O$_{12}$ have been constructed with the lanthanide dopant energy levels by utilizing spectroscopic data. The Ce^{3+} 5d excited states are calculated by first principle calculations. Thermoluminescence (TL) glow curves of (Ce^{3+}, Sm^{3+}) co-doped (Sr, Ca)$_3$(Y, Lu)$_2$Ge$_3$O$_{12}$ samples show a good agreement with the prediction of lanthanide trapping depths derived from the energy level diagram. Finally, the energy level diagram is used to explain the low thermal quenching temperature of Ce^{3+} and the absence of afterglow in (Sr, Ca)$_3$(Y, Lu)$_2$Ge$_3$O$_{12}$.

1. Introduction

The spectroscopic properties of lanthanide doped phosphors depend not only on the energy differences between 4f and 5d states but also on the location of these states relative to the electronic states of the host, i.e. the conduction band (CB) and the valence band (VB)[1].

Lanthanide energy levels are of great interest both for an application and for a theoretical point of view. Thermal quenching of 5d-4f emission occurs when the electron in the 5d excited state like in Ce^{3+} or Eu^{2+} transfers to the conduction band[2-4]. This is not beneficial to LED phosphors since such thermal ionization will dramatically reduce the efficiency of the phosphors at the LED working temperature[5] (~150°C). On the other hand, afterglow phosphors need a relatively low thermal quenching temperature to spontaneously ionize sun light excited 5d electrons to the conduction band to be captured by the traps[6-8].

The lanthanide trap depths can be predicted and analyzed by locating the ground state $4f^n$ levels relative to the host bands[9]. When divalent lanthanide $4f^n$ ground state levels are close to the CB the corresponding trivalent ions may act as electron trapping centers. Bos *et al* confirmed this hypothesis by studying the thermoluminescence of $YPO_4:Ce^{3+},Ln^{3+}$ (Ln= Pr, Nd, Sm, Dy, Ho, Er, Tm and Yb) samples and found that for each lanthanide co-dopant there is a different trap depth[10]. The trap depth in this case is the distance between divalent lanthanide ground state $4f^n$ levels and the bottom of the CB.

The trivalent lanthanide $4f^n$ ground state levels can be close above the VB, which means that these ions may act as hole trapping centers. Chakrabarti[11] *et al* reported that samarium acts as a recombination centre and cerium the trapping centre that capture holes after UV irradiation in $MgS:Ce^{3+},Sm^{3+}$. Recently, Luo[12] *et al* systematically studied the hole trapping and hole release processes in $GdAlO_3:Ln^{3+}$, RE^{3+} (Ln=Sm, Eu and Yb, RE= Ce, Pr and Tb), and found that RE co-dopants act as the hole trapping centres where the trap depth relates to the distance between trivalent lanthanide 4f lowest states to the top of the VB.

Initially $(Sr, Ca)_3(Y, Lu)_2Ge_3O_{12}$ garnets doped with Ce^{3+} as luminescence center and other trivalent lanthanides as electron trapping center were selected for study with the aim to develop persistent luminescence phosphors. Ce^{3+} in garnet compounds emit in the green to red and have strong absorption of day light[13-15]. However, the materials turn out not to be good persistent luminescence phosphors. To explain this we determined the electronic structure providing the location of the lanthanide levels within the band gap.

The materials share a normal garnet structure $A_3B_2C_3O_{12}$ (cation occupy 24 c, 16 a, and 24 d), where A, B and C denote dodecahedral (point symmetry 222), octahedral (point symmetry $\bar{3}$) and tetrahedral (point symmetry $\bar{4}$) coordination, respectively[16-17]. The crystal chemistry of garnets is detailed discussed by S. Geller, which covers more than hundreds of garnet compounds[18]. However, few reports are found for this family of garnets. Uhlich *et al* reported that the Eu^{3+} enters the octahedral Y site with an O^{2-}-Eu^{3+} charge transfer band at ~240 nm[19]. Kalaji *et al* studied the room temperature spectroscopy of Ce^{3+} doped $(Sr, Ca)_3(Y, Lu)_2Ge_3O_{12}$ garnets and concluded that Ce^{3+} enters the dodecahedral site instead of the octahedral one[20].

Kaminskii *et al* mentioned that in the two-cation garnets the RE^{3+} dopant mainly enters the dodecahedral site and in some cases it can also enter the octahedral site[21].

Obviously, something is still not fully clear in this type of materials. For instance, what is the site occupancy of Eu^{3+} and Ce^{3+} in $(Sr, Ca)_3(Y, Lu)_2Ge_3O_{12}$ garnets? Secondly, where are the Ce^{3+} ground states and the 5d excited states in $(Sr, Ca)_3(Y, Lu)_2Ge_3O_{12}:Ce^{3+}$ with respect to the host valence and conduction bands? Thirdly, how does the bandgap change by replacing the Sr or Y by the smaller Ca or Lu ions and how does this influence the Ce^{3+} 5d bands and Eu^{3+} charge transfer energy?

The objective of this study is to systematically reveal the lanthanide levels in $(Sr, Ca)_3(Y, Lu)_2Ge_3O_{12}$ garnets to answer the above questions. First-principles calculations and the empirical chemical shift model are combined to determine the electronic structure and construct the energy level diagrams showing the lanthanide levels within the band gap[9]. The electronic structures of $(Sr, Ca)_3(Y, Lu)_2Ge_3O_{12}$ host lattices are calculated by using the hybrid density functional theory (DFT) method. The $4f_1$ and $5d_1$ energy levels of Ce^{3+} are calculated by a wave function-based multi-reference approach. The low-temperature VUV photoluminescence excitation and emission spectra for the undoped $(Sr, Ca)_3(Y, Lu)_2Ge_3O_{12}$ host lattices and the photoluminescence for Ce^{3+} or Eu^{3+} doped samples are presented. The experimental results for Ce^{3+} doped samples are used to compare with theoretical calculations to identify the Ce^{3+} site occupancy and the 5d levels. Low-temperature thermoluminescence measurements are carried out for (Ce^{3+}, Sm^{3+}) co-doped samples to locate the Sm^{2+} ground state. Results are used to construct the energy level diagram of $(Sr, Ca)_3(Y, Lu)_2Ge_3O_{12}$ showing the locations of the lanthanide states within the band gap.

2. Experimental and theoretical methods

2.1. Experimental Details

All starting materials were purchased from Sigma-Aldrich and used without further treatment. The appropriate stoichiometric mixture of GeO_2 (99.99%), $SrCO_3$ (99.99%), $CaCO_3$ (99.99%) and rare earth oxides with the purity of 5N (99.999%) were weighed according to the chemical formula and milled homogeneously with the help of acetone. Then the powders were synthesized at 1300 °C for 12 hours in a corundum crucible in an atmosphere of N_2. After cooling down, the as-prepared materials were grinded again and synthesized at 1300 °C for another 12 hours in the same atmosphere. Finally, the obtained compounds were cooled down to room temperature.

All powders were checked with a PANalytical XPert PRO X-ray diffraction system with Co Kα (λ = 0.178901 nm) X-ray tube (45 kV, 40 mA). The photoluminescence excitation (PLE) and photoluminescence emission (PL) measurement were measured with a set-up that consists of an UV/VIS branch with a 500W Hamamatsu CW Xe lamp and Gemini 180 monochromator and a VUV/UV branch using a deuterium lamp with an ARC VM502 vacuum monochromator. The Perkin Elmer MP-1913 photomultiplier was exploited as a detector connected at the exit slit of a Princeton Acton SP2300 monochromator. The sample was placed in an evacuated sample chamber.

Low temperature thermoluminescence (LTTL) measurements (90-450 K) were recorded with a sample chamber operating under vacuum (P = 10^{-7} mbar), a $^{90}Sr/^{90}Y$ beta irradiation source having a dose rate of ~0.4 mGy s^{-1} and a Perkin-Elmer channel PM tube (MP-1393). Liquid nitrogen was used as a cooling medium. A 490 nm bandpass filter (490FS10-50) was placed between the sample and PMT during the measurements to select only Ce^{3+} emission. The peak intensities were corrected for mass differences.

2.2. Computational Details

The Ce-doped $Sr_3Y_2Ge_3O_{12}$ and $Ca_3Y_2Ge_3O_{12}$ crystals were modeled by using a unit cell containing 160 atoms, in which one of the 16 Y atoms, or one of the 24 Sr or Ca atoms was replaced by a Ce. The lattice parameters and atomic coordinates of the doped unit cell were optimized by periodic DFT calculations using a hybrid exchange-correlation functional in the PBE0 scheme, as implemented in the VASP code[22-23]. The excess charge of Ce^{3+} on the Sr^{2+} or Ca^{2+} site was compensated by introducing a uniform background charge density, and the spurious Coulomb interaction in charged supercells is expected to be small due to the large size of the supercells[24]. The electrons of Ce ($5s^25p^64f^15d^16s^2$), Ca ($3s^23p^64s^2$), Sr ($4s^24p^64s^2$), Y ($4s^24p^64d^15s^2$), Ge ($4s^24p^2$) and O ($2s^22p^4$) were treated as valence electrons, and their interactions with the respective cores were described by the projected augmented wave (PAW) method[25]. The geometry optimizations were performed until the total energies and the Hellmann–Feynman forces on the atoms converged to 10^{-6} eV and 0.01 eV $Å^{-1}$, respectively. Due to the large size of the systems and the high computational cost of hybrid DFT with plane wave basis, only one k-point (Γ point) was used to sample the Brillouin zone, with a cutoff energy of 530 eV for the plane wave basis.

The $4f_1$ and $5d_1$ energy levels of Ce^{3+} were computed with a wave function-based embedded cluster approach. On the basis of the atomic structures optimized by hybrid DFT, the

Ce-centered clusters were constructed, each comprising the central Ce^{3+}, the oxygen ions in the first coordination shell, and the closest Ge^{4+} ions in the second coordination shell. Their immediate surroundings within a sphere of radius 10.0 Å were represented by several hundreds of *ab initio* model potentials (AIMPs)[26] and the remainder of the surroundings were simulated by tens of thousands of point charges at lattice sites, which are generated with Lepetit's method[27]. Wave function-based CASSCF/CASPT2 calculations with the spin-orbit effect were then carried out to obtain the $4f^1$ and $5d^1$ energy levels of Ce^{3+} by using the program MOLCAS[28]. In the CASSCF calculations, a [4f, 5d, 6s] complete active space was adopted, and in the CASPT2 calculations, the dynamic correlation effects of the Ce^{3+} 5s, 5p, 4f, 5d electrons and the O^2 2s, 2p electrons were considered. Further details about the basis sets can be found in Refs. 29-31.

3. Results

3.1 X-Ray diffraction and photoluminescence spectroscopy of $(Sr, Ca)_3(Y, Lu)_2Ge_3O_{12}$

XRD patterns of synthesized $(Sr, Ca)_3(Y, Lu)_2Ge_3O_{12}$ phosphors are shown in Figure 1. All samples are of single phase and match very well with the $Sr_3Y_2Ge_3O_{12}$ reference card (No. 1408217) due to their same crystal structure (space group: Ia-3d). A slight shift of the XRD peaks can be observed in Figure 1b due to different lattice parameters among the as-prepared materials.

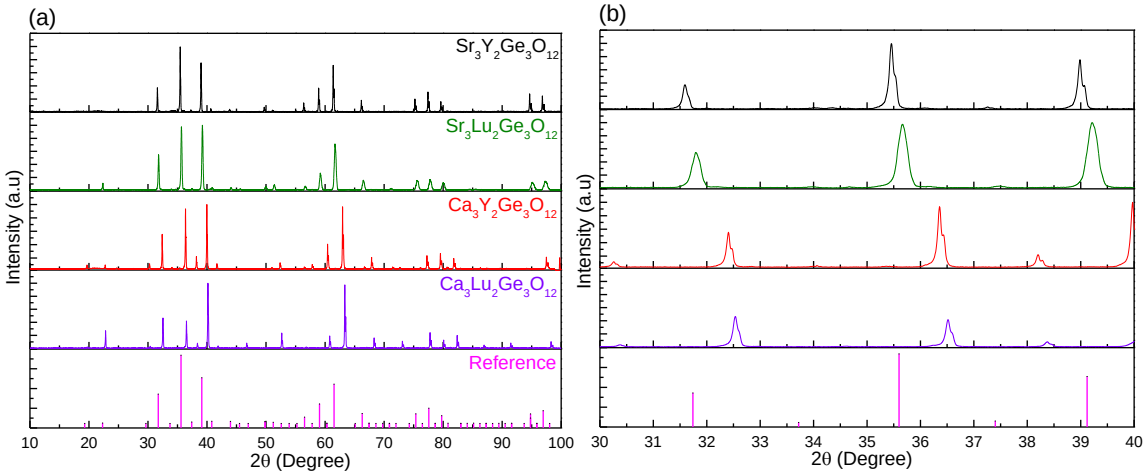

Figure 1. (a) XRD patterns of the as-prepared samples of $Sr_3Y_2Ge_3O_{12}$, $Sr_3Lu_2Ge_3O_{12}$, $Ca_3Y_2Ge_3O_{12}$ and $Ca_3Lu_2Ge_3O_{12}$. (b) Detailed XRD patterns in the range from 30 to 40°.

Figure 2 shows the low temperature VUV excitation and emission spectra of $(Sr, Ca)_3(Y, Lu)_2Ge_3O_{12}$ host lattices. The host excitation maximum of $Sr_3Y_2Ge_3O_{12}$ and $Sr_3Lu_2Ge_3O_{12}$ are both reached at 5.9 eV (210 nm) indicating that they have the same bandgap. The reason is that $Sr_3Y_2Ge_3O_{12}$ and $Sr_3Lu_2Ge_3O_{12}$ samples have very close lattice parameters, which can be observed from Figure 1(b) that the XRD peak positions for these two samples are at almost the same position. For the $Ca_3Y_2Ge_3O_{12}$ and $Ca_3Lu_2Ge_3O_{12}$, the exciton creation energy is 6.1 eV (200 nm). The emission from 300 to 400 nm of $(Sr, Ca)_3(Y, Lu)_2Ge_3O_{12}$ host lattices shown in Figure 1b are all from a sort of charge transfer emission like host exciton or defect trapped exciton emission. However, the precise origin is unknown.

Figure 3 shows the photoluminescence excitation and emission spectra of Eu^{3+} single doped $Sr_3Y_2Ge_3O_{12}$. There are two different excitation bands at 280 nm (hereafter referred as the charge transfer band CT) and 235 nm (hereafter referred as the near defect exciton band NDE) when monitored at 610 nm and 597 nm emission, respectively. The reasons for assignments will become clear in the discussion section. Typical Eu^{3+} line emission with different $^5D_0$-$^7F_1$ and $^5D_0$-$^7F_2$ relative intensity is found with different excitation energy. The $^5D_0$-$^7F_2$ hypersensitive forced electronic-dipole transition is dominating when excited by 280 nm UV irradiation. This indicates that the Eu^{3+} ions are at a non-inversion symmetry site[32]. On the other hand, the $^5D_0$-$^7F_1$ magnetic-dipole transition is dominating when excited by 235 nm UV light, indicating the Eu^{3+} ions at an inversion symmetry site[32].

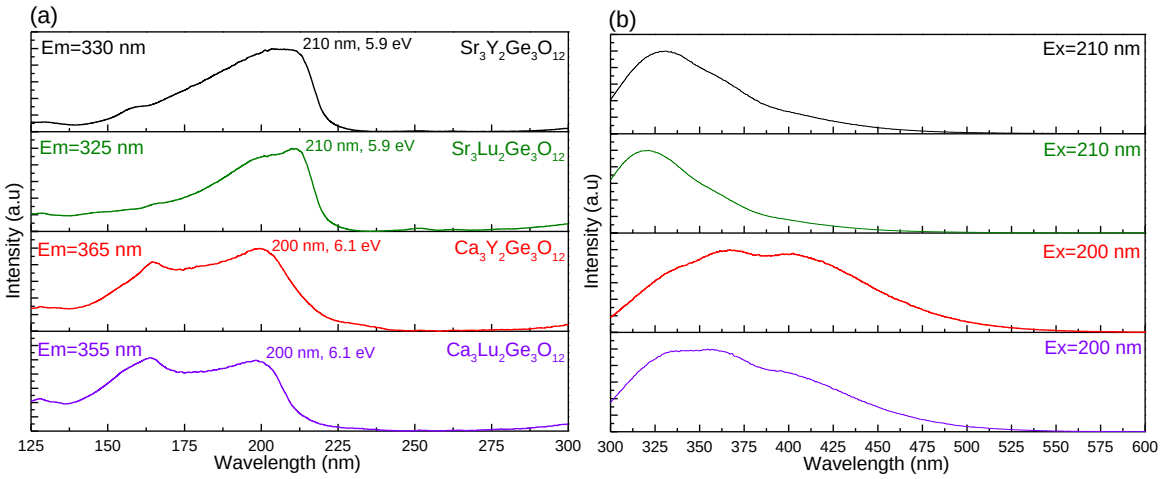

Figure 2. (a) PLE and (b) PL spectra of $Sr_3Y_2Ge_3O_{12}$, $Sr_3Lu_2Ge_3O_{12}$, $Ca_3Y_2Ge_3O_{12}$ and $Ca_3Lu_2Ge_3O_{12}$ host lattices. The spectra were measured by deuterium lamp excitation. The excitation spectra were recorded at the emission bands maximum and the emission spectra were excited at the excitation maxima, which are shown in the figure legend. All measurements were performed at 10 K.

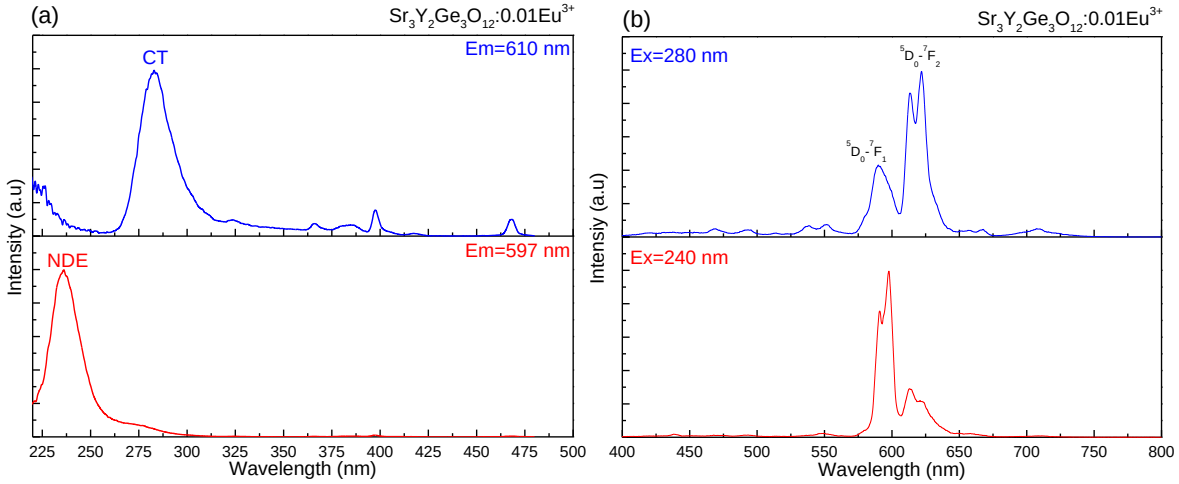

Figure 3. Site selective excitation (a) and emission (b) spectra of $Sr_3Y_2Ge_3O_{12}$:0.01Eu^{3+}. All measurements were performed at RT.

Figures S1, S2 and S3 show the two excitation and emission spectra for the other three garnet compounds. They also indicate that the Eu^{3+} dopants are at two different sites. Table 1 lists the wavelength maxima of the CT and NDE bands. We observe that the CT band shifts to higher energy from $Sr_3Y_2Ge_3O_{12}$ to $Ca_3Lu_2Ge_3O_{12}$ while the NDE band stays at almost the same position.

Table 1 The excitation band maxima of Eu^{3+} single doped samples

	CT-band	NDE-band
$Sr_3Y_2Ge_3O_{12}$:Eu^{3+}	280 (4.43 eV)	235 (5.27 eV)
$Sr_3Lu_2Ge_3O_{12}$:Eu^{3+}	265 (4.68 eV)	232 (5.34 eV)

$Ca_3Y_2Ge_3O_{12}:Eu^{3+}$	260 (4.77 eV)	235 (5.27 eV)
$Ca_3Lu_2Ge_3O_{12}:Eu^{3+}$	255 (4.86 eV)	233 (5.32 eV)

Figure 4 and 5 show the PLE and PL spectra of Ce^{3+} single doped $(Sr, Ca)_3(Y, Lu)_2Ge_3O_{12}$ phosphors recorded at 10 K. The PLE and PL spectra of $Sr_3Y_2Ge_3O_{12}:Ce^{3+}$ measured at room temperature is displayed in Figure S4, and it does not show much difference to the low temperature spectra.

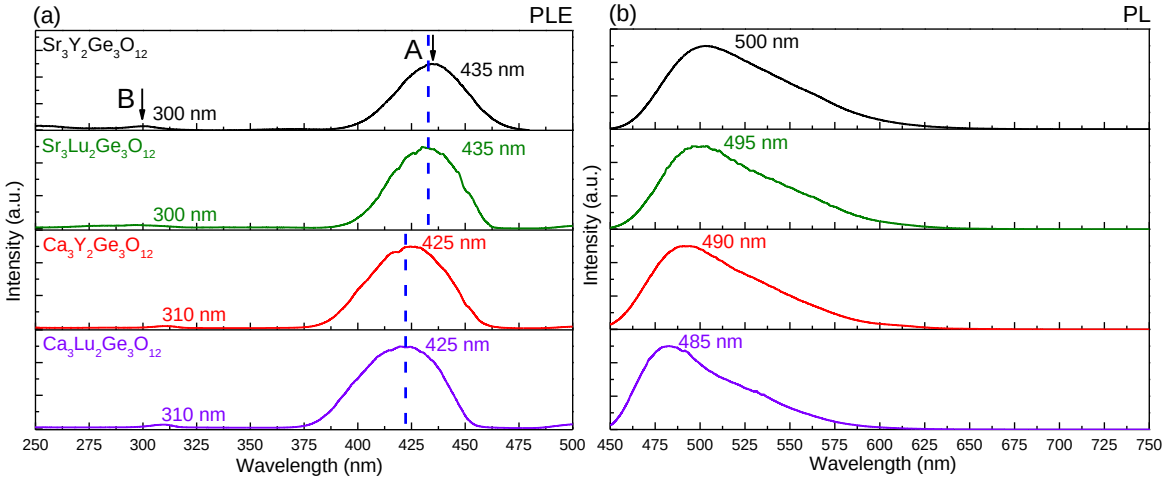

Figure 4. (a) PLE and (b) PL spectra of $Sr_3Y_2Ge_3O_{12}:0.01Ce^{3+}$, $Sr_3Lu_2Ge_3O_{12}:0.01Ce^{3+}$, $Ca_3Y_2Ge_3O_{12}:0.01Ce^{3+}$ and $Ca_3Lu_2Ge_3O_{12}:0.01Ce^{3+}$. The excitation spectra were recorded at the emission peak maxima, and the emission spectra were excited at the Band A peak maxima. All the measurements were carried out at 10 K.

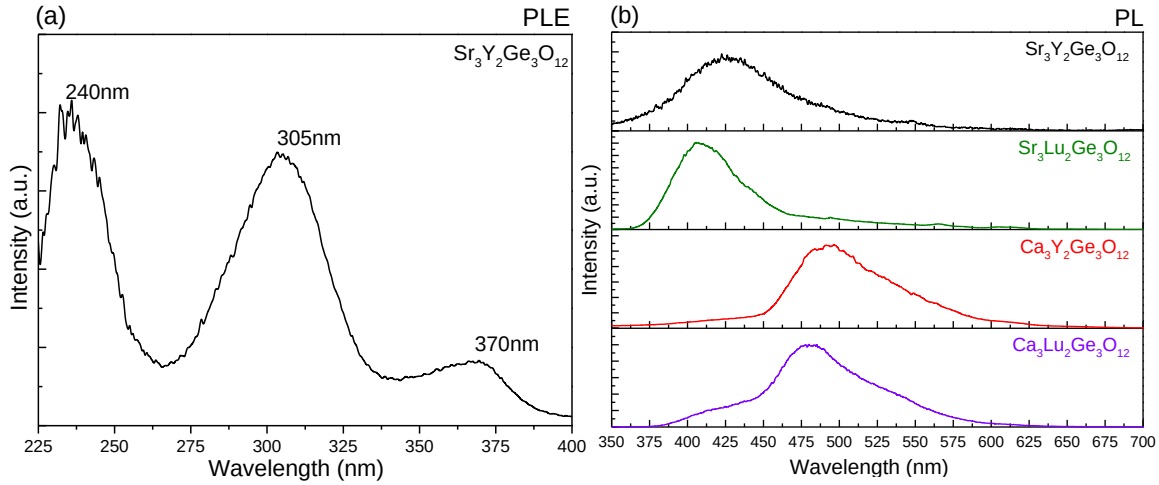

Figure 5. (a) PLE spectrum of $Sr_3Y_2Ge_3O_{12}:0.01Ce^{3+}$ monitored at 425 nm. (b) PL spectra of $Sr_3Y_2Ge_3O_{12}:0.01Ce^{3+}$, $Sr_3Lu_2Ge_3O_{12}:0.01Ce^{3+}$, $Ca_3Y_2Ge_3O_{12}:0.01Ce^{3+}$ and $Ca_3Lu_2Ge_3O_{12}:0.01Ce^{3+}$ excited by 300 nm UV irradiation. All the measurements were carried out at 10 K.

The excitation spectra in Figure 4 ranging from 250 to 500 nm are composed of two bands: one intense band in the blue range (420-435 nm, Band A) and one weak band in the UV range (300-315 nm, Band B). A broad emission band centered at ~500 nm can be observed for all

the samples when excited at Band A maxima, and it is composed of the two unresolved Ce^{3+} $5d_1$-$^2F_{5/2}$ and $5d_1$-$^2F_{7/2}$ emission bands. When excited by 300 nm UV irradiation, a new band centered at ~ 425 nm appears for all samples shown in Figure 5(b). A representative excitation spectrum of $Sr_3Y_2Ge_3O_{12}:Ce^{3+}$ monitored at 425 nm emission is shown in Figure 5(a). It seems that Ce^{3+} occupies two different sites.

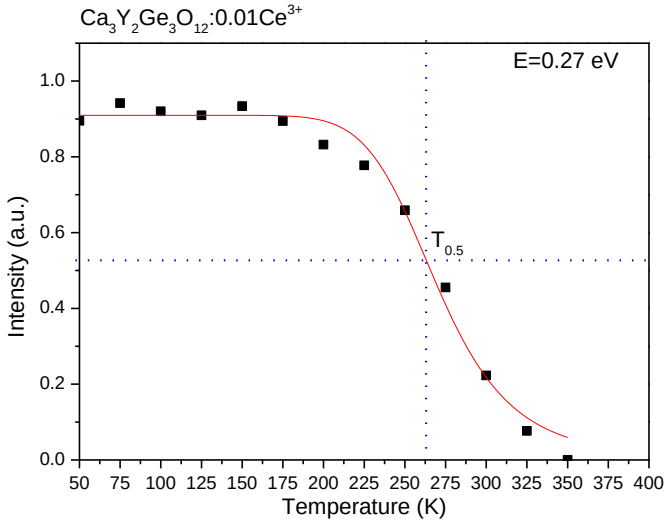

Figure 6. Temperature dependence of $Ca_3Y_2Ge_3O_{12}:0.01Ce^{3+}$. The excitation monometer was set as 425 nm. The solid curve through the data is a fitted curve. The measurement was carried out by a liquid helium cryostat.

Figure 6 shows the thermal quenching curve of $Ca_3Y_2Ge_3O_{12}:0.01Ce^{3+}$ from 50 to 350 K. The quenching temperature ($T_{0.5}$) where intensity has reduced by 50% is at ~265 K. The activiation energy for thermal quenching can be derived from[33]:

$$I(T) = \frac{I(0)}{1+C\exp(-\frac{E}{kT})} \quad (1)$$

Where *I (T)* and *I (0)* is the intensity at temperature T and 50 K, *k* is the Boltzmann constant. A fit through the data in Figure 6, as indicated by the solid curve provides *E* = 0.27 eV, which is indicative for the energy difference between the $5d^1$ state and the bottom of the CB.

3.2 Thermoluminescence glow curves of $(Sr, Ca)_3(Y, Lu)_2Ge_3O_{12}:Ce^{3+},Sm^{3+}$

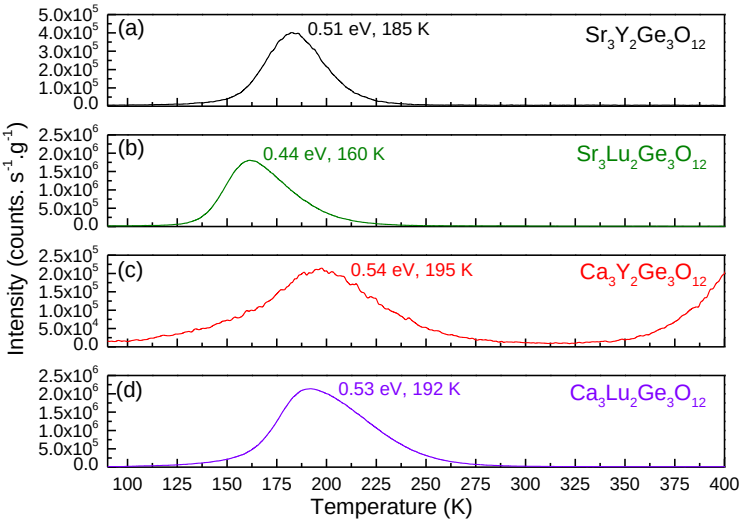

Figure 7. Low temperature thermoluminescence (LTTL) glow curves of (a) $Sr_3Y_2Ge_3O_{12}:0.01Ce^{3+},0.01Sm^{3+}$, (b) $Sr_3Lu_2Ge_3O_{12}:0.01Ce^{3+},0.01Sm^{3+}$, (c) $Ca_3Y_2Ge_3O_{12}:0.01Ce^{3+},0.01Sm^{3+}$ and (d) $Ca_3Lu_2Ge_3O_{12}:0.01Ce^{3+},0.01Sm^{3+}$. All measurements were carried out with the low-temperature TL setup from 90 to 450 K after 1600 s irradiation by its β source. The heating rate was 1 K/s for all TL-recordings. The TL glow curves were measured with a 490 nm bandpass filter (490FS10-50) to transmit the 5d-4f Ce^{3+} emission (at ~ 500 nm).

In Figure 7 the calibrated LTTL glow curves from Ce^{3+} 5d-4f emission in (Ce^{3+}, Sm^{3+}) co-doped $(Sr, Ca)_3(Y, Lu)_2Ge_3O_{12}$ are shown. Several co-doping combinations of (Ce^{3+}, Sm^{3+}), (Ce^{3+}, Eu^{3+}), (Ce^{3+}, Tm^{3+}) and (Ce^{3+}, Yb^{3+}) were tried but only the (Ce^{3+}, Sm^{3+}) combination gives TL within this measurement range. The temperature T_m where TL is maximum depends on the host lattice and ranges from 160 K for $Sr_3Lu_2Ge_3O_{12}$: Ce^{3+}, Sm^{3+} to 200 K for $Ca_3Y_2Ge_3O_{12}$: Ce^{3+}, Sm^{3+}.

The trap depth E of the Sm^{3+} trapping centre in (Ce^{3+}, Sm^{3+}) co-doped $(Sr, Ca)_3(Y, Lu)_2Ge_3O_{12}$ were determined using the T_m from Figure 7 and employing[34]

$$\frac{\beta E}{kT_m^2} = s\ \exp(-\frac{E}{kT_m}) \qquad (2)$$

where β = 1K s^{-1} is the heating rate, k is the Boltzmann constant, and s is the frequency factor[34]. The frequency factor s, which is related to the host lattice vibrational mode, is estimated using the most intense vibrational energy for trigonal GeO_2 ($P3_221$) of 444 cm^{-1} ($1.3x10^{13}$ s^{-1})[35-36], where Ge has the same coordination number as in $(Sr, Ca)_3(Y, Lu)_2Ge_3O_{12}$ (for both CN=4). We assumed a similar value for our samples due to a similar $[GeO_4]^{4-}$ group present. The estimated trap depth values can be found in Figure 7.

3.3 First Principle Calculations

The atomic structures of the representative pure $Sr_3Y_2Ge_3O_{12}$ and $Ca_3Y_2Ge_3O_{12}$ unit cells were optimized using hybrid DFT with the standard PBE0 functional containing 25% HF exchange. The calculated lattice constants were compared with the experimental ones reported in literatures (Table S1)[37-38].

On the basis of the optimized atomic structures, the band gaps were calculated by using the same DFT functional with a modified PBE0 hybrid functional. The percentage of HF exchange was changed until optimal correspondences with the experimental values are obtained, with 32% HF exchange[39-40]. The modified PBE0 functional gives band gap values of 6.33 eV for $Sr_3Y_2Ge_3O_{12}$ and 6.53 eV for $Ca_3Y_2Ge_3O_{12}$, to be compared with the experimental values (6.37 for $Sr_3Y_2Ge_3O_{12}$ and 6.60 eV for $Ca_3Y_2Ge_3O_{12}$). Those experimental values are from the exciton creation peaks in Figure 2. To account for the exciton binding energy, a mobility band gap of $1.08*E_{ex}$ was assumed [9].

Figure 8 shows the total and orbital-projected densities of states (DOSs) for the $Sr_3Y_2Ge_3O_{12}$ and $Ca_3Y_2Ge_3O_{12}$ unit cells. The Fermi levels at the top of the valence band are set at 0 eV. The VB of both samples are formed primarily by O 2p orbitals. The bottom of the conduction band for both compounds is composed of discrete peaks, for which an enlarged view is shown in the insets. The CB edge state is constituted by a small peak at 6.33 eV for $Sr_3Y_2Ge_3O_{12}$ and 6.53 eV for $Ca_3Y_2Ge_3O_{12}$, which is mainly derived from s-character states of Ge and O atoms and d-character states of Y and Sr/Ca atoms. The other discrete peaks have additional contributions from p-character states of O and Ge atoms. Above these, the conduction band consists mainly of Y d, Sr/Ca d, and O p states.

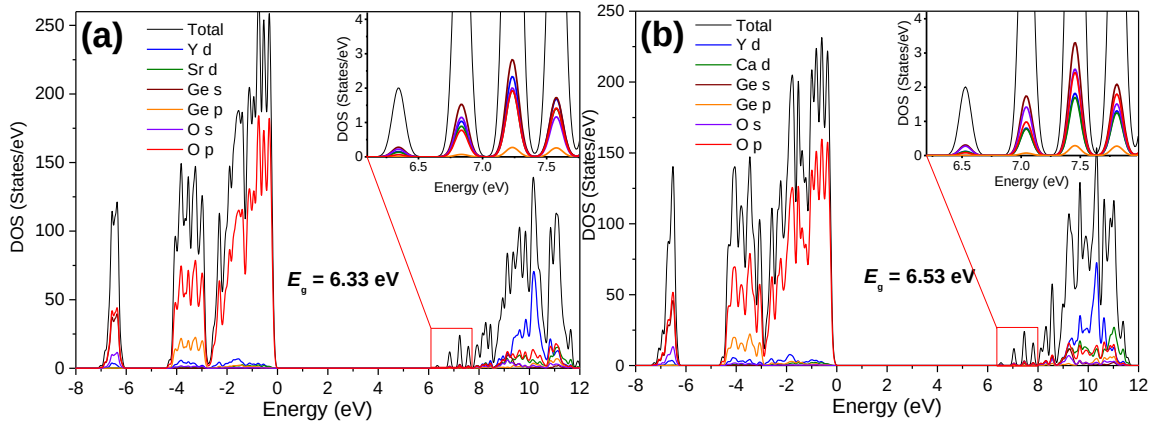

Figure 8. Total and orbital-projected DOSs for the (a) $Sr_3Y_2Ge_3O_{12}$ and (b) $Ca_3Y_2Ge_3O_{12}$ unit cells calculated by DFT with the PBE0 hybrid functional containing 32% HF exchange and a 2×2×2 k-point grid to sample the Brillouin zone. The enlarged views of the DOS for the edge of conduction bands are shown in the inset.

Relative to the DOS at the energy of the deeper Y 4s states (below -40 eV) in $Sr_3Y_2Ge_3O_{12}$, we observe that, the valence band of $Ca_3Y_2Ge_3O_{12}$ moves downward by 0.13 eV, while the conduction band moves upward by 0.07 eV, giving rise to a 0.2 eV larger band gap.

The Ce^{3+} 4f → $5d_{1\text{-}5}$ transition energies were calculated by wave-function-based CASSCF/CASPT2 functions with spin-orbit coupling. The relative intensity of the 5d-4f transitions are calculated by RASSI−SO wave functions and the energies at the spin-orbit level[41]. Calculations were performed for Ce on the dodecahedral Sr and Ca site and for Ce on the octahedral Y site. The results are listed in Table 2, and a comparison with experimental data from Figure 4(a) and 5(a) are shown in Figure 9. For Ce^{3+} in octahedral and dodecahedral sites, the two sets of calculated energy levels are quite different both for 4f and 5d level energies.

Table 2. Calculated energy levels of $4f^1$ and $5d^1$ configurations for the Ce^{3+} in $Sr_3Y_2Ge_3O_{12}$ and $Ca_3Y_2Ge_3O_{12}$ at different sites. All the units are wavenumber (cm^{-1}).

	$Sr_3Y_2Ge_3O_{12}$				$Ca_3Y_2Ge_3O_{12}$			
	Ce_{Sr}	5d->4f intensities	Ce_Y	5d->4f intensities	Ce_{Ca}	5d->4f intensities	Ce_Y	5d->4f intensities
$4f_1$	0		0		0		0	
$4f_2$	124		1151		204		1204	
$4f_3$	881		1276		879		1283	
$4f_4$	2263		2378		2370		2372	
$4f_5$	2380		3558		2384		3586	
$4f_6$	2866		3669		2882		3735	
$4f_7$	3668		4293		3844		4356	
$5d_1$	26423	1.00	24446	1.00	26830	1.00	23828	1.00
$5d_2$	33791	0.09	25049	0.84	32437	0.44	24443	0.54
$5d_3$	43869	1.07	26124	0.05	46196	1.16	25797	0.14
$5d_4$	48218	0.11	58522	0.20	48478	0.26	58728	0.15
$5d_5$	51756	0.28	58530	0.25	51763	0.22	58870	0.26

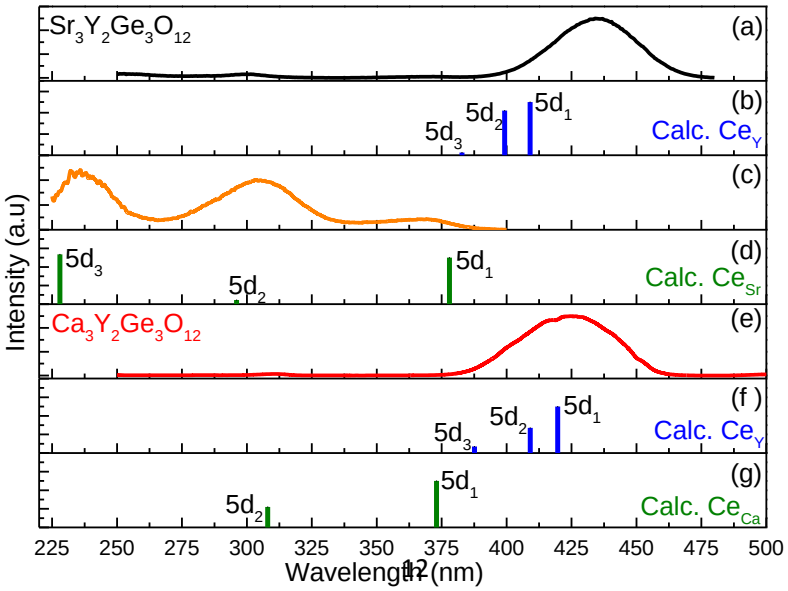

Figure 9. Schematic representation of the calculated energies of the 4f-5d transitions of Ce^{3+} on the octahedral (Y) and the dodecahedral site (Sr/Ca) sites for $Sr_3Y_2Ge_3O_{12}$ and $Ca_3Y_2Ge_3O_{12}$. (a) PLE spectrum of $Sr_3Y_2Ge_3O_{12}$:0.01Ce^{3+} monitored at 500 nm. (b) Calculated Ce^{3+} 5d levels for $Sr_3Y_2Ge_3O_{12}$:0.01Ce^{3+} at the Y site. (c) PLE spectrum of $Sr_3Y_2Ge_3O_{12}$:0.01Ce^{3+} monitored at 425 nm. (d) Calculated Ce^{3+} 5d levels for $Sr_3Y_2Ge_3O_{12}$:0.01Ce^{3+} at the Sr site. (e) PLE spectrum of $Ca_3Y_2Ge_3O_{12}$:0.01Ce^{3+} monitored at 490 nm. (f) Calculated Ce^{3+} 5d levels for $Ca_3Y_2Ge_3O_{12}$:0.01Ce^{3+} at the Y site. (g) Calculated Ce^{3+} 5d levels for $Ca_3Y_2Ge_3O_{12}$:0.01Ce^{3+} at the Ca site.

4. Discussion

We will first deal with the question raised in the introduction regarding the site occupancy followed by the questions regarding location of the lanthanide levels with respect to the host bands and how that changes with type of host garnet.

4.1 Eu^{3+} charge transfer band and the site occupancy

The Eu^{3+} charge transfer (CT) energy defines the energy to transfer an electron from the top of the valence band to Eu^{3+} which then becomes divalent[42]. Therefore, the Eu^{3+} CT energy provides the location of the Eu^{2+} ground state above the VB[43]. The vacuum referred electron binding energy in the Eu^{2+} ground state appears within the chemical shift model always near -4 eV in oxides [39, 40]. This means that the Eu^{3+} CT energy gives direct information about the position of the VB maximum. The first principle calculation showed that the VB of $Ca_3Y_2Ge_3O_{12}$ moves downward by 0.13 eV with respect to that of $Sr_3Y_2Ge_3O_{12}$ if aligned by the Y 4s states. This calculation is consistent with Table 1 where the excitation bands in column 2 shifts towards about 0.1-0.2 eV higher energy when Sr is replaced by the smaller Ca or Y by the smaller Lu. Therefore, we assign the 280 nm band in Figure 3 as the CT band, and the same for Figure S1, S2 and S3. The excitation band in column three of Table 1 that remains at almost the same position is assigned to a near defect exciton (NDE) band.

For Eu^{3+} we found evidence in Figure 3 and S1-S3 for emission from a site with and without inversion symmetry. In $(Sr, Ca)_3(Y, Lu)_2Ge_3O_{12}$ host lattice, the dodecahedral site is the non-inversion site (due to the 222 point symmetry) while the octahedral site is the site with the inversion symmetry (due to the $\bar{3}$ point symmetry). This explains the difference relative intensity of $^5D_0$-$^7F_1$ and $^5D_0$-$^7F_2$ transition. On the other hand, when the trivalent Eu^{3+} enters into the divalent site, intrinsic charge compensation is needed. The extra positive charge introduced by Eu^{3+} may generate defects like interstitial oxygen or cation vacancies (V_{Sr} or V_Y) that will change the Sr (Ca)-O bond length and the polyhedral shape surrounding Sr (Ca), leading to a non-inversion symmetry environment.

4.2 Ce^{3+} 4f-5d excited levels and site occupancy

Kalaji *et al*[20] attribute the excitation bands in the UV and blue regions as shown in Figure 4 to the transitions from the $^2F_{5/2}$ ground state to the lowest two 5d excited states from Ce^{3+} assumed to be located at the dodecahedral site. This was motivated by the observation that replacing Y^{3+} with Lu^{3+} barely affects the excitation spectrum and only slightly blue shifts the emission[20]. The one-site occupancy hypothesis cannot explain the extra emission band centred at ~425 nm when excited by 300 nm UV light (Figure 5). We attribute the 300 nm excitation band and the blue emission bands to a second Ce^{3+} site. In order to confirm this, the theoretical Ce^{3+} 5d excited states were calculated to analyse the Ce^{3+} site occupancy and excitation spectra.

Table 2 compiles the calculated Ce^{3+} 5d energies at the two different sites and Figure 9 visualizes it. From the correspondence between experiment and calculations we attribute the lowest broad energy excitation band (Band A) observed experimentally to the triplet $4f_1 \rightarrow 5d_{1\text{-}3}$ transitions of Ce^{3+} located at the octahedral site. The three 4f → 5d transitions merge

into one single broad excitation band. The crystal field splitting between the $5d_1$ and $5d_5$ level for Ce^{3+} at this site are calculated as about 34100 cm^{-1} (4.22 eV) and 35050 cm^{-1} (4.34 eV) for $Sr_3Y_2Ge_3O_{12}$ and $Ca_3Y_2Ge_3O_{12}$. We note that discrepancies exist between the calculated and experimental $4f_1 \rightarrow 5d_{1\text{-}3}$ transitions of Ce^{3+}, which could be due to errors in the calculated local structure of Ce^{3+} at the Y^{3+} site of $Sr_3Y_2Ge_3O_{12}$.

The weak higher energy excitation band (Band B) in Figure 4 cannot be assigned to the doublet e-band for Ce^{3+} on an octahedral site which is predicted at much higher energy according to the calculation (Table 2). Next to band B, Figure 5a reveals two other excitation bands when monitoring emission at 425 nm in $Sr_3Y_2Ge_3O_{12}:Ce^{3+}$. Based on the agreement with the calculated energies for the 4f-5d bands for Ce on the dodecahedral site in Figure 9c and 9d all three excitation bands and the ~425nm emission band are attributed to Ce^{3+} on the dodecahedral site. The calculated data explain why the Ce^{3+} $4f \rightarrow 5d_{4\text{-}5}$ transitions for Ce^{3+} on both sites are not experimentally observed because excitation energies are higher than the bandgap energy.

In Figure 4, the $5d_1$ band for Ce in the octahedral site blue shifts from 435 nm to 425 nm while the $5d_2$ band for Ce in the dodecahedral site red shifts from 300 nm to 310 nm for $Sr_3Y_2Ge_3O_{12}:Ce^{3+}$ and $Ca_3Y_2Ge_3O_{12}:Ce^{3+}$. Applying the empirical crystal field splitting equation $\varepsilon_{cfs}=\beta_{poly}R^{-2}$, where β_{poly} refers to the type of polyhedron that surrounds Ce^{3+} and R means the average bond length of Ce^{3+} to the nearby bonded anions (O^{2-} here)[44]. We know that for a certain polyhedron type, the shorter the bond length the larger the crystal field splitting will be. Table S2 shows that the bond length of Y-O in $Ca_3Y_2Ge_3O_{12}$ (2.3330 Å) is longer than that in $Sr_3Y_2Ge_3O_{12}$ (2.2494 Å). This suggests that the Ce^{3+} CFS at the octahedral site in $Ca_3Y_2Ge_3O_{12}$ will be smaller than in $Sr_3Y_2Ge_3O_{12}$, leading the blue shift of the A band. The Ca (Ce)-O average bond length in $Ca_3Y_2Ge_3O_{12}$ (2.5150 Å) is shorter than of Sr (Ce)-O (2.6174 Å), and apparently a stronger CFS leads to the red shift of the B band.

4.3 Energy level diagrams of $(Sr, Ca)_3(Y, Lu)_2Ge_3O_{12}$

We intend to construct a diagram where the binding energy of an electron in lanthanide defect states and in the host valence band and conduction band states can be compared with respect to one and the same energy reference. Usually, like in XPS and UPS studies and in ab initio and full principle calculations[45-46], energies are referred to the top of the valence band which is then set as the zero of energy like in Figure 8 of this work. However, with such approach one cannot relate the binding energies in different compounds, like the four garnets of this work, to a common reference of energy. There are only a few solutions to this problem. In the field of semi-conductor science the valence band offset at the hetero-junction of two compounds can be determined[47-48]. In the field of electro-chemistry, valence band energies can be related to the standard hydrogen potential[49-50]. In the field of luminescence science, the chemical shift model, was developed in 2012 to construct a vacuum referred binding energy (VRBE) diagram that makes it possible to compare the binding at the VB maximum in different compounds with respect to a same reference energy. VRBE is defined as the energy needed to bring an electron from a level in the diagram to the vacuum outside the sample. The

energy at rest in vacuum or vacuum level is then defined as energy zero. Further details about the VRBE diagram can be found in Refs. 1 and 9.

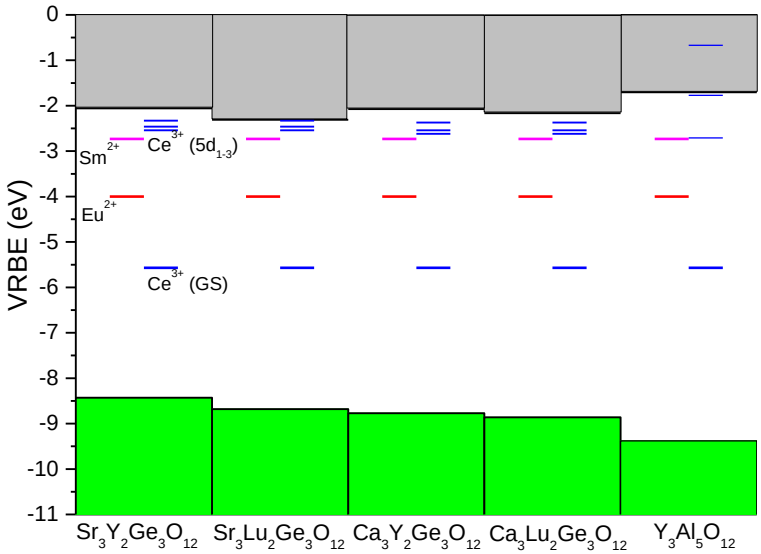

Figure 10. VRBE diagram of $(Sr, Ca)_3(Y, Lu)_2Ge_3O_{12}$ and $Y_3Al_5O_{12}$ with location of Ce^{3+}, Eu^{2+}, and Sm^{2+} levels.

Figure 10 shows stacked VRBE diagrams for $(Sr, Ca)_3(Y, Lu)_2Ge_3O_{12}$ with location of Ce^{3+}, Eu^{2+}, and Sm^{2+} levels. The detailed VRBE diagrams with all lanthanide impurity levels are shown in Figure S5 in the Supporting Information. The data used to construct the diagrams are listed in Table 3. We adopted a value of 6.73 eV for the so-called U-parameter in the chemical shift model for all four garnet compounds in this work. This translates to a VRBE value of -3.98 eV for Eu^{2+}, -2.73 eV for Sm^{2+}, and -5.42 eV for Ce^{3+} [51-52]. The charge transfer energy of Eu^{3+} in $(Sr, Ca)_3(Y, Lu)_2Ge_3O_{12}$ as was shown in Table 1 then provides the energy at the top of the VB. The decrease of the charge transfer energy of Eu^{3+} implies that the valence band energy moves upward. The bandgap energy was obtained from Figure 2 by adding 8% to the exciton banding energy in order to account for the electron hole binding energy in the exciton. The VRBE in the 5d states of Ce^{3+} was obtained by adding the calculated 5d energies in Table 2 for octahedral Ce^{3+} to the ground state energies. The VRBE in the Ce^{3+} 5d levels for $Sr_3Lu_2Ge_3O_{12}$ and $Ca_3Lu_2Ge_3O_{12}$ are the same as in $Sr_3Y_2Ge_3O_{12}$ and $Ca_3Y_2Ge_3O_{12}$, respectively, due to similar excitation spectra. The $Y_3Al_5O_{12}$ VRBE diagram is added for comparison and the data comes from Ref.53.

Inspecting the VRBE for the valence band and the conduction band of $(Sr, Ca)_3(Y, Lu)_2Ge_3O_{12}$, Figure 10 shows that the VB maxima go downwards while the CB minima go slightly upward except for $Sr_3Lu_2Ge_3O_{12}$ with decreasing the unit cell volume. The binding energies of the electrons in anions usually increase when the bond length to the coordinating ions decreases, which is a manifestation of the Madelung field. For $(Sr, Ca)_3(Y, Lu)_2Ge_3O_{12}$, the top of the VB is composed of O 2p orbitals. Therefore, on replacing Sr or Y by smaller Ca or Lu the bond length with O anions decreases and that promotes stronger O 2p shell electron binding energy as observed in Figure 10. The VRBE scheme is consistent with the calculated

data where it was found that the VB moves downward by 0.13 eV from $Sr_3Y_2Ge_3O_{12}$ to $Ca_3Y_2Ge_3O_{12}$ as compared to the energy of deep Y 4s orbitals (below -40 eV).

The CB bottoms in the $(Sr, Ca)_3(Y, Lu)_2Ge_3O_{12}$ garnets are on average at ~0.45 eV higher energy than in $Y_3Al_5O_{12}$. The VRBE scheme shows that the energy between the Ce^{3+} $5d_1$ level and the CB in $(Sr, Ca)_3(Y, Lu)_2Ge_3O_{12}$ is ~0.5 eV lower than in $Y_3Al_5O_{12}:Ce^{3+}$. It is well established, and particularly so for $Y_3Al_5O_{12}$ by Ueda *et al.*, that the quenching of Ce^{3+} 5d-4f emission is caused by thermal ionization of the 5d electron to the conduction band. Ueda *et al* and Weber *et al* reported that the thermal quenching temperature ($T_{0.5}$) is 643 K and 650 K, respectively[54-55]. The quenching temperature $T_{0.5}$ ~265 K for $Ca_3Y_2Ge_3O_{12}:Ce^{3+}$ in Figure 6 and corresponding 0.27 eV activation energy (ΔE) is ~0.5 eV lower than in $Y_3Al_5O_{12}:Ce^{3+}$ (0.77 eV). This is consistent with the VRBE diagram showing that the Ce^{3+} $5d_1$ in $Ca_3Y_2Ge_3O_{12}$ is 0.55 eV lower than in $Y_3Al_5O_{12}$ value. The low lying conduction band in the germanium based garnets is then the reason for the lower thermal quenching temperature of $(Sr, Ca)_3(Y, Lu)_2Ge_3O_{12}:Ce^{3+}$ as compared to the aluminate based garnet $Y_3Al_5O_{12}:Ce^{3+}$.

Table 3 The parameters to construct the VRBE diagram of $(Sr,Ca)_3(Y,Lu)_2Ge_3O_{12}$ and $Y_3Al_5O_{12}$. The units for all the parameters are eV.

Compound	E^{ex}	E^{CT}	E_V	E_C	$E_{Sm^{2+}}$	$E_{Ce^{3+}}$ (GS)	$E_{Ce^{3+}}$ ($5d_1$)	$E_{Ce^{3+}}$ ($5d_2$)	$E_{Ce^{3+}}$ ($5d_3$)	$E_{Ce^{3+}}$ ($5d_4$)	$E_{Ce^{3+}}$ ($5d_5$)
$Sr_3Y_2Ge_3O_{12}$	6.37	4.43	-8.43	-2.06	-2.73	-5.42	-2.54	-2.46	-2.33	1.69	1.69
$Sr_3Lu_2Ge_3O_{12}$	6.37	4.68	-8.68	-2.31	-2.73	-5.42	-2.54	-2.46	-2.33	1.69	1.69
$Ca_3Y_2Ge_3O_{12}$	6.59	4.77	-8.77	-2.07	-2.73	-5.42	-2.62	-2.54	-2.37	1.71	1.73
$Ca_3Lu_2Ge_3O_{12}$	6.59	4.86	-8.86	-2.16	-2.73	-5.42	-2.62	-2.54	-2.37	1.71	1.73
$Y_3Al_5O_{12}$	7.10	5.42	-9.38	-1.71	-2.73	-5.42	-2.71	-1.77	-0.67	0.08	0.62

For the TL-studies on Ce-Sm, Ce-Eu, Ce-Tm, and Ce-Yb co-doped samples, only the one with (Ce^{3+}, Sm^{3+}) co-doping showed a TL signal in the range of 90 to 450 K, see Figure 7. The VRBE diagram of Figure 10 and Figure S5 predict that of all the lanthanides only the ground state of divalent Sm, Eu and Yb will be below the CB. This indicates that the corresponding trivalent ions may act as electron traps and since the ground state of Ce^{3+} is above the valence band it will act as a hole trapping center. The trap depths from the VRBE diagrams listed in Table 3 for Sm^{2+} are 0.67, 0.42, 0.66 and 0.57 eV for (Ce^{3+}, Sm^{3+}) co-doped $Sr_3Y_2Ge_3O_{12}$, $Sr_3Lu_2Ge_3O_{12}$, $Ca_3Y_2Ge_3O_{12}$ and $Ca_3Lu_2Ge_3O_{12}$, respectively. These values are close to the trap depths derived from the thermoluminescence glow curves in Figure 7, which are 0.51, 0.44, 0.54 and 0.53 eV, respectively. This confirms that Sm^{3+} co-dopant acts as the electron trapping center and since the TL glow is from Ce who acts as the hole trapping and the recombination center. The same phenomenon is also reported in lanthanides co-doped $YPO_4:Ce^{3+}$ [56-57], $GdAlO_3:Ce^{3+}$ [12]and $Y_3Al_5O_{12}:Ce^{3+}$ [58]. In these cases, Ce^{3+} acts as the recombination center as well as the hole trapping center while the lanthanide co-dopants act as electron trapping centers.

The trap depth of Yb^{2+} is always 0.81 eV deeper than that of Sm^{2+}, and for the four garnet compounds has an average value of ~1.43 eV (Figure S5). Adopting the frequency factor of

$1.3x10^{13}$ s^{-1} and a heating rate of 1K/s, the TL peak maxium temperature calculated with Eq. (2), is ~503 K. Figure 6 shows that at this TL temperature the Ce^{3+} emission is totally quenched. For Eu^{3+} co-doped samples, the Eu^{2+} trap depths are even 0.3 eV deeper than for Yb^{2+} this is the reason of the absence of TL glow peaks for (Ce^{3+}, Yb^{3+}) and (Ce^{3+}, Eu^{3+}) co-doping combinations.

5. Conclusion

Photoluminescence spectroscopy and first principle calculations were simultaneously performed in this research. Eu^{3+} and Ce^{3+} are found located at both dodecahedral and octahedral sites from the photoluminescence spectroscopy. Calculated data on 4f-5d transition energies for Ce^{3+} on both sites are consistent with the photoluminescence experimental results. The studied germanium based garnets are found to have ~1 eV smaller bandgap than the yttrium aluminate garnet. The VRBE schemes reveal that the conduction bands of the studied germanium based garnets are at ~0.5 eV lower energy and the valence bands at ~0.5 eV higher energy than the yttrium aluminate garnet. A clear trend is observed that the valence band goes downwards with decreasing the unit cell volume. The lower lying conduction band causes a lower quenching temperature for the Ce^{3+} emission. Only Sm^{3+} as co-dopant provides a TL glow and other co-dopant lanthanides either cannot trap an electron or trap the electron too deep so that the recombination luminescence on Ce^{3+} will be quenched. The experimental spectroscopic results, the first principle calculations and the vacuum referred binding energies derived from the chemical shift model all provide a mutually consistent interpretation of the electron, luminescent, and trapping properties of the studied germanium based garnets. The combination of the experiments, first-principle calculations and the semi-empirical chemical shift model can be used as an alternative method to screen the luminescence materials for certain application (for instance, LED phosphors, afterglow, etc.) and to understand the luminescence mechanisms.

6. Acknowledgements:

This research is supported by the Dutch Technology Foundation (STW), which is the applied science division of NWO, and the Technology program of the Ministry of Economic Affairs.
L. N. acknowledges support from the National Natural Science Foundation of China (Grant Nos. 11574003, 11174005).

7. Supporting Information:

Including PLE and PL spectra of Eu^{3+} single doped $Sr_3Lu_2Ge_3O_{12}$, $Ca_3Y_2Ge_3O_{12}$ and $Ca_3Lu_2Ge_3O_{12}$, room temperature photoluminescence spectroscopy of $Sr_3Y_2Ge_3O_{12}$:0.01Ce^{3+}, the low temperature (10K) PLE spectra of Ce^{3+} single doped $(Sr, Ca)_3(Y, Lu)_2Ge_3O_{12}$ excited at 300 nm, comparison of the experimental and calculated lattice parameters and band gap, the lattice parameters for $(Sr, Ca)_3Y_2Ge_3O_{12}$ and $Y_3Al_5O_{12}$ host lattices, the detail VRBE diagram of $(Sr, Ca)_3(Y, Lu)_2Ge_3O_{12}$.

Reference

1. Dorenbos, P., A Review on How Lanthanide Impurity Levels Change with Chemistry and Structure of Inorganic Compounds. *ECS Journal of Solid State Science and Technology*., **2013**, 3001-3011.
2. Shao, Q.; Lin, H.; Dong, Y.; Fu, Y.; Liang, C.; He, J.; Jiang, J., Thermostability and Photostability of Sr3SiO5:Eu2+ Phosphors for White Led Applications. *J. Solid State Chem.*, **2015**, *225*, 6, 72–77.
3. Joos, J. J.; Dirk, P.; Smet, P. F., Energy Level Modeling of Lanthanide Materials: Review and Uncertainty Analysis. *Phys. Chem. Chem. Phys.,* **2015**, 17, 19058-19078.
4. Dorenbos, P., Thermal Quenching of Eu2+ 5d–4f Luminescence in Inorganic Compounds. *J. Phys.: Condens. Matter.,* **2005**, *17*, 8103-8111.
5. Yeh, C.-W.; Chen, W.-T.; Liu, R.-S.; Hu, S.-F.; Sheu, H.-S.; Chen, J.-M.; Hintzen, H. T., Origin of Thermal Degradation of Sr2–XSi5N8:Eux Phosphors in Air for Light-Emitting Diodes. *J. Am. Chem. Soc.* **2012**, *134*, 14108-14117.
6. Ueda, J.; Dorenbos, P.; Bos, A.; Kuroishi, K.; Tanabe, S., Control of Electron Transfer between Ce3+ and Cr3+ in Y3Al5-XGaxO12 Host by Conduction Band Engineering. *J. Mater. Chem. C.,* **2015**, *3*, 5642-5651.
7. Dorenbos, P., Mechanism of Persistent Luminescence in Eu2+ and Dy3+ Codoped Aluminate and Silicate Compounds. *J. Electrochem. Soc*., **2005**, *152*, H107-H110.
8. Li, Y.; Gecevicius, M.; Qiu, J., Long Persistent Phosphors-from Fundamentals to Applications. *Chem. Soc. Rev*., **2016**, *45,* 2090-2136.
9. Dorenbos, P., Modeling the Chemical Shift of Lanthanide 4f Electron Binding Energies. *Phys. Rev. B*., **2012**, *85*,165107-165117.
10. Bos, A. J. J.; Dorenbos, P.; Bessière, A.; Lecointre, A.; Bedu, M.; Bettinelli, M.; Piccinelli, F., Study of Tl Glow Curves of Ypo4 Double Doped with Lanthanide Ions. *Radiat. Meas*., **2011**, *46*, 1410-1416.
11. Chakrabarti, K.; Mathur, V. K.; Rhodes, J. F.; Abbundi, R. J., Stimulated Luminescence in Rare - Earth Doped Mgs. *J. Appl. Phys.,* **1988**, *64*, 1363-1366.
12. Luo, H.; Bos, A. J. J.; Dorenbos, P., Controlled Electron–Hole Trapping and Detrapping Process in GdAlO3 by Valence Band Engineering. *J. Phys. Chem. C.*, **2016**, *120*, 5916-5925.
13. Zhong, J.; Zhuang, W.; Xing, X.; Liu, R.; Li, Y.; Liu, Y.; Hu, Y., Synthesis, Crystal Structures, and Photoluminescence Properties of Ce3+ Doped Ca2LaZr2Ga3O12: New Garnet Green-Emitting Phosphors for White Leds. *J. Phys. Chem. C.*, **2015**, *119*, 5562-5569.
14. Chen, L., et al., Charge Deformation and Orbital Hybridization: Intrinsic Mechanisms on Tunable Chromaticity of Y3Al5O12:Ce3+ Luminescence by Doping Gd3+ for Warm White Leds. *Sci. Rep*., **2015**, *5*, 11514-11531.
15. Setlur, A. A.; Heward, W. J.; Gao, Y.; Srivastava, A. M.; Chandran, R. G.; Shankar, M. V., Crystal Chemistry and Luminescence of Ce3+-Doped Lu2CaMg2(Si,Ge)3O12 and Its Use in Led Based Lighting. *Chem. Mater*., **2006**, *18*, 3314-3322.
16. Luo, H.; Liu, J.; Zheng, X.; Xu, B.; Lu, Y.; Han, L.; Ren, K.; Yu, X., Synthesis and Luminescence Properties of Mg–Si Co-Doped Tb3Al5O12:Ce3+ Phosphors with Blue Excitation for White Leds. *J. Am. Ceram. Soc.* **2012**, *95*, 3582-3587.
17. Novak, G. A.; Gibbs, G. V., The Crystal Chemistry of the Silicate Garnets. *THE AMERICAN MINERALOGIST.,* **1971**, *56*, 791-825.
18. Geller, S., Crystal Chemistry of the Garnets. *Zeitschrift für Kristallographie-Crystalline Materials* **1967**, *125*, 1-47.
19. Uhlich, D.; Plewa, J.; Jüstel, T., Phase Formation and Characterization of Sr3Y2Ge3O12,

Sr3In2Ge3O12, and Ca3Ga2Ge3O12 Doped by Trivalent Europium. *J. Lumin.,* **2008**, *128*, 1649-1654.

20. Kalaji, A.; Saines, P. J.; George, N. C.; Cheetham, A. K., Photoluminescence of Cerium-Doped (Ca1−XSrx)3RE2Ge3O12 Garnet Phosphors for Solid State Lighting: Relating Structure to Emission. *Chem. Phys. Lett.,* **2013**, *586*, 91-96.

21. Kaminskii, A. A.; Mill, B. V.; Butashin, A. V., Growth and Stimulated Emission Spectroscopy of Ca3Ga2Ge3O12:Nd3+ Garnet Crystals. *physica status solidi (a).,* **1983**, *78*, 723-732.

22. Kresse, G.; Furthmüller, J., Efficient Iterative Schemes for Ab Initio Total-Energy Calculations Using a Plane-Wave Basis Set. *Phys. Rev. B.,* **1996**, *54*, 11169-11186.

23. Kresse, G.; Joubert, D., From Ultrasoft Pseudopotentials to the Projector Augmented-Wave Method. *Phys. Rev. B.,* **1999**, *59*, 1758-1775.

24. Freysoldt, C.; Grabowski, B.; Hickel, T.; Neugebauer, J.; Kresse, G.; Janotti, A.; Van de Walle, C. G., First-Principles Calculations for Point Defects in Solids. *Rev. Mod. Phys*., **2014**, *86*, 253-305.

25. Blöchl, P. E., Projector Augmented-Wave Method. *Phys. Rev. B.,***1994**, *50*, 17953-17979.

26. Barandiarán, Z.; Seijo, L., The Abinitio Model Potential Representation of the Crystalline Environment. Theoretical Study of the Local Distortion on Nacl:Cu+. *J. Chem. Phys.,* **1988**, *89*, 5739-5746.

27. Gellé, A.; Lepetit, M.-B., Fast Calculation of the Electrostatic Potential in Ionic Crystals by Direct Summation Method. *J. Chem. Phys.,* **2008**, *128*, 244716-244724.

28. Karlström, G., et al., Molcas: A Program Package for Computational Chemistry. *Comput. Mater. Sci.,* **2003**, *28*, 222-239.

29. Barandiarán, Z.; Seijo, L., The Abinitio Model Potential Method. Cowan–Griffin Relativistic Core Potentials and Valence Basis Sets from Li (Z = 3) to La (Z = 57). *Can. J. Chem.,* **1992**, *70*, 409-415.

30. Muñoz-García, A. B.; Seijo, L., Structural, Electronic, and Spectroscopic Effects of Ga Codoping on Ce-Doped Yttrium Aluminum Garnet: First-Principles Study. *Phys. Rev. B.,* **2010**, *82*, 184118-184128.

31. Ning, L.; Lin, L.; Li, L.; Wu, C.; Duan, C.-k.; Zhang, Y.; Seijo, L., Electronic Properties and 4f - 5d Transitions in Ce-Doped Lu2SiO5: A Theoretical Investigation. *J. Mater. Chem.,* **2012**, *22*, 13723-13731.

32. Lee, K.-G.; Yu, B.-Y.; Pyun, C.-H.; Mho, S.-I., Vacuum Ultraviolet Excitation and Photoluminescence Characteristics of (Y,Gd)Al3(Bo3)4:Eu3+. *Solid State Commun.,* **2002**, *122*, 485-488.

33. Wintle, A. G., Thermal Quenching of Thermoluminescence in Quartz. *Geophys. J. Int.,* **1975**, *41*, 107-113.

34. Azorín, J., Determination of Thermoluminescence Parameters from Glow Curves—I. A Review. *International Journal of Radiation Applications and Instrumentation. Part D. Nuclear Tracks and Radiat. Meas.,* **1986**, *11*, 159-166.

35. Shinde, S. L.; Nanda, K. K., Thermal Oxidation Strategy for the Synthesis of Phase-Controlled Geo2 and Photoluminescence Characterization. *CrystEngComm.,* **2013**, *15*, 1043-1046.

36. Micoulaut, M.; Cormier, L.; Henderson, G. S., The Structure of Amorphous, Crystalline and Liquid GeO2. *J. Phys.: Condens. Matter*., **2006**, *18*, R753-R784.

37. Marin, S. J.; O'Keeffe, M.; Young Jr, V. G.; Von Dreele, R. B., The Crystal Structure of Sr3y2ge3o12. *J. Solid State Chem.* **1991**, *91*, 173-175.

38. Levy, D.; Barbier, J., Normal and Inverse Garnets: Ca3Fe2Ge3O12, Ca3Y2Ge3O12 and Mg3Y2Ge3O12. *Acta Crystallographica Section C.,* **1999**, *55*, 1611-1614.

39. Ning, L.; Zhou, C.; Chen, W.; Huang, Y.; Duan, C.; Dorenbos, P.; Tao, Y.; Liang, H., Electronic Properties of Ce3+-Doped Sr3Al2O5Cl2: A Combined Spectroscopic and Theoretical Study. *J. Phys. Chem. C.,* **2015**, 12, 6785-6792.

40. Shi, R.; Qi, M.; Ning, L.; Pan, F.; Zhou, L.; Zhou, W.; Huang, Y.; Liang, H., Combined Experimental and Ab Initio Study of Site Preference of Ce3+ in SrAl2O4. *J. Phys. Chem. C.,* **2015**, *119*, 19326-19332.

41. Ning, L.; Wu, C.; Li, L.; Lin, L.; Duan, C.; Zhang, Y.; Seijo, L., First-Principles Study on Structural Properties and 4f → 5d Transitions of Locally Charge-Compensated Ce3+ in CaF2. *J. Phys. Chem. C.,* **2012**, *116*, 18419-18426.

42. Liu, X.; Li, L.; Noh, H. M.; Moon, B. K.; Choi, B. C.; Jeong, J. H., Chemical Bond Properties and Charge Transfer Bands of O2--Eu3+, O2--Mo6+ and O2--W6+ in Eu3+-Doped Garnet Hosts Ln3M5O12 and AbO4 Molybdate and Tungstate Phosphors. *Dalton Trans.,* **2014**, *43*, 8814-8825.

43. Dorenbos, P., The Charge Transfer Energy and the Relation with the Band Gap of Compounds. *J. Lumin.,* **2005**, *111*, 89-104.

44. Dorenbos, P., Crystal field splitting of lanthanide 4fn−15d-levels in inorganic compounds. *J. Alloys Compd.,* **2002**, *341*, 156-159.

45. Huang, B., Native Point Defects in Cas: Focus on Intrinsic Defects and Rare Earth Ion Dopant Levels for up-Converted Persistent Luminescence. *Inorg. Chem.,* **2015**, 54, 11423-11440.

46. De Vos, A.; Lejaeghere, K.; Vanpoucke, D. E. P.; Joos, J. J.; Smet, P. F.; Hemelsoet, K., First-Principles Study of Antisite Defect Configurations in ZnGa2O4:Cr Persistent Phosphors. *Inorg. Chem.,* **2016**, *55*, 2402-2412.

47. Caldas, M. J.; Fazzio, A.; Zunger, A., A Universal Trend in the Binding Energies of Deep Impurities in Semiconductors. *Appl. Phys. Lett.,* **1984**, *45*, 671-673.

48. Wei, S.-H.; Zunger, A., Role of D Orbitals in Valence-Band Offsets of Common-Anion Semiconductors. *Phys. Rev. Lett.,* **1987**, *59*, 144-147.

49. Xiaobo Chen, S. S., Liejin Guo, and Samuel S. Mao, Semiconductor-Based Photocatalytic Hydrogen Generation. *Chem. Rev.,* **2010,** *110*, 6503–6570.

50. van de Krol, R.; Liang, Y.; Schoonman, J., Solar Hydrogen Production with Nanostructured Metal Oxides. *J. Mater. Chem.,* **2008**, *18*, 2311-2320.

51. Dorenbos, P., The Electronic Level Structure of Lanthanide Impurities in REPO4 , REBO3 , REAlO3 , and RE2O3 (Re = la, Gd, Y, Lu, Sc) Compounds. *J. Phys.: Condens. Matter.,* **2013**, *25*, 225501-225508.

52. Dorenbos, P., The Electronic Structure of Lanthanide Doped Compounds with 3d, 4d, 5d, or 6d Conduction Band States. *J. Lumin.,* **2014**, *151*, 224-228.

53. Dorenbos, P., Electronic Structure and Optical Properties of the Lanthanide Activated RE3(Al1−XGax)5O12 (Re=Gd, Y, Lu) Garnet Compounds. *J. Lumin.,* **2013**, *134*, 310-318.

54. Ueda, J.; Dorenbos, P.; Bos, A. J. J.; Meijerink, A.; Tanabe, S., Insight in the Thermal Quenching Mechanism for Y3Al5O12:Ce3+ through Thermoluminescence Excitation Spectroscopy. *J. Phys. Chem. C.,* **2015**, 119, 25003-25008.

55. Weber, M. J., Nonradiative Decay from 5d States of Rare Earths in Crystals. *Solid State Commun.,* **1973**, *12*, 741-744.

56. Krumpel, A. H.; Bos, A. J. J.; Bessière, A.; van der Kolk, E.; Dorenbos, P., Ontrolled Electron and Hole Trapping in YPO4:Ce3+,Ln3+ and LuPO4:Ce3+,Ln3+ (Ln=Sm, Dy, Ho, Er, Tm). *Phys. Rev. B.,* **2009**, *80*, 085103-085113.

57. Dorenbos, P.; Bos, A. J. J.; Poolton, N. R. J., Carrier Recombination Processes and Divalent Lanthanide Spectroscopy in YPO4:Ce3+;L3+ (L=Sm,Dy,Tm). *Phys. Rev. B.,* **2010**, *82, 195127-195134*.

58. You, F.; Bos, A. J. J.; Shi, Q.; Huang, S.; Dorenbos, P., Thermoluminescence Investigation of Donor Ce3+, Pr3+, Tb3+ Acceptor Eu3+, Yb3+ Pairs in Y3Al5O12. *Phys. Rev. B.,***2012**, *85*, 115101-115108.

Table of Contents Image